nature catalysis

ARTICLES

https://doi.org/10.1038/s41929-022-00804-4

Check for updates

Cation-doped ZnS catalysts for polysulfide conversion in lithium–sulfur batteries

Zihan Shen[1], Xin Jin[2], Jiaming Tian[2], Matthew Li[3], Yifei Yuan[3], Shuo Zhang[2], Susu Fang[4], Xing Fan[2], Weigao Xu[4], Hong Lu[2], Jun Lu[3]✉ and Huigang Zhang[1]✉

Catalytic conversion of polysulfides is regarded as a crucial approach to enhancing kinetics and suppressing the shuttle effect in lithium–sulfur (Li–S) batteries. However, the activity prediction of Li–S catalysts remains elusive owing to the lack of mechanistic understanding of activity descriptors. Here, we report a volcano-shaped relationship between polysulfide adsorption ability and catalytic activity. In conjunction with theoretical analysis, we distinguish catalytic and anchoring effects to delineate the role of adsorption and emphasize the passivation of catalysts. These findings enable us to develop a composite catalyst, $Co_{0.125}Zn_{0.875}S$, which shows higher performance than simple binary compounds. Such a fundamental understanding of the intrinsic link between polysulfide adsorption and catalytic activity offers a rational viewpoint for designing Li–S catalysts and tuning their activities.

The lithium–sulfur (Li–S) system is regarded as one of the most promising candidates for next-generation rechargeable batteries because of its high specific energy (2,600 W h kg^{-1}), the high abundance of sulfur resources, low cost and environmental compatibility[1,2]. However, practical implementation of Li–S batteries is hindered by the sluggish kinetics of sulfur cathodes[3,4], low reversibility of Li metal anodes[5,6] and the shuttle effect[7,8] (soluble polysulfides migrate from the cathode to anode, lowering sulfur utilization and corroding Li metal as shown in Fig. 1a). Among these drawbacks, the slow kinetics of polysulfide (Li_2S_n, $1 \leq n \leq 8$) conversion play a critical role in determining the electrochemical performance of Li–S batteries[9,10] as they are closely coupled to other issues, especially exacerbating polysulfide shuttling and lowering the cyclability of batteries. Catalytic conversion of polysulfides not only enhances the kinetics of Li–S batteries but also suppresses the shuttle effect[11]. Previous studies added metal oxides[12,13], sulfides[14], phosphides[15] and nitrides[16] to sulfur cathodes to adsorb polysulfides or reportedly catalyse the conversion reaction. High catalytic activity is usually correlated to the strong adsorption of polysulfides on catalysts[17]. Although the intrinsic link between adsorption and catalytic activity is not well resolved in theory, these pioneering studies[12–22] demonstrated that using catalysts in sulfur cathodes has been able to modestly or significantly improve the electrochemical properties of Li–S batteries.

To further improve or develop new catalysts, some mechanistic approaches have been proposed recently. Duan and co-workers[23] fabricated N- and S-doped graphene catalysts to lower the activation energy for improving the kinetics of polysulfide conversion. Li and co-workers[24] reported an intercalation-conversion composite cathode to immobilize polysulfides and unlock their high gravimetric capacity. Altering the band structure of catalysts can increase the binding energy of polysulfides and accelerate surface electron exchange for a fast redox reaction[25,26]. A large variety of materials has been reported to successfully catalyse polysulfide conversion. However, the contemporary methodology for catalyst development relies more or less on trial and error. For example, all three intermediate compounds (CoS_2 (ref. [27]), Co_3S_4 (ref. [28]) and Co_9S_8 (ref. [29])) in the Co–S binary system had reportedly demonstrated catalytic activity for Li–S batteries owing to the strong binding energies of polysulfides on cobalt sulfides. How to design better catalysts beyond simple binary compounds needs the in-depth understanding of the intrinsic linkage between the experimentally demonstrated catalytic activities and theoretically calculated binding energies of polysulfides. However, such a mechanistic study on catalysts is lacking, especially at the atomic and molecular levels, which limits the rational design and activity tuning of catalysts for Li–S batteries.

In this Article, we report a fundamental study on how the adsorption of polysulfides determines catalytic activity. By examining the activity of a series of transition metal dopants (Mn^{2+}, Fe^{2+}, Co^{2+}, Ni^{2+} or Cu^{2+}) in a ZnS lattice, we found that strengthening adsorption does not necessarily lead to the enhancement of catalytic activity. Especially when the desorption of discharged polysulfides (Li_2S_2/Li_2S) is rate limiting, the strong adsorption of Li_2S_2/Li_2S may induce the passivation of catalysts. Only medium adsorption of polysulfides can enhance the conversion of Li_2S_4 and meanwhile facilitate the desorption of Li_2S_2/Li_2S (Fig. 1b), thereby showing the highest catalytic activity. A volcano trend is revealed between activity and adsorption strength. Using this correlation, we were able to develop a highly efficient catalyst, $Co_{0.125}Zn_{0.875}S$. The resultant Li–S battery shows an ultralow capacity fading rate of 0.033% per cycle over 1,500 cycles at a 2C rate. At a high sulfur loading (7 mg cm^{-2}), the Li–S battery using $Co_{0.125}Zn_{0.875}S$ can maintain a high capacity of 513.2 mAh g^{-1} at 1C for over 200 cycles. Such a high activity has not been achieved by simple binary compounds. The revealed connection between adsorption and catalysis as an activity-tuning strategy offers a rational viewpoint to analyse polysulfide conversion and design efficient catalysts. In consideration of the relatively high cost and limited availability of cobalt resources, these design principles could be further applied to developing cobalt-free catalysts in the future.

[1]State Key Laboratory of Multiphase Complex Systems, Institute of Process Engineering, Chinese Academy of Sciences, Beijing, China. [2]National Laboratory of Solid State Microstructures, Collaborative Innovation Center of Advanced Microstructures, College of Engineering and Applied Sciences, Nanjing University, Nanjing, China. [3]Chemical Sciences and Engineering Division, Argonne National Laboratory, Lemont, IL, USA. [4]Key Laboratory of Mesoscopic Chemistry, School of Chemistry and Chemical Engineering, Nanjing University, Nanjing, China. ✉e-mail: junlu@anl.gov; hgzhang@ipe.ac.cn

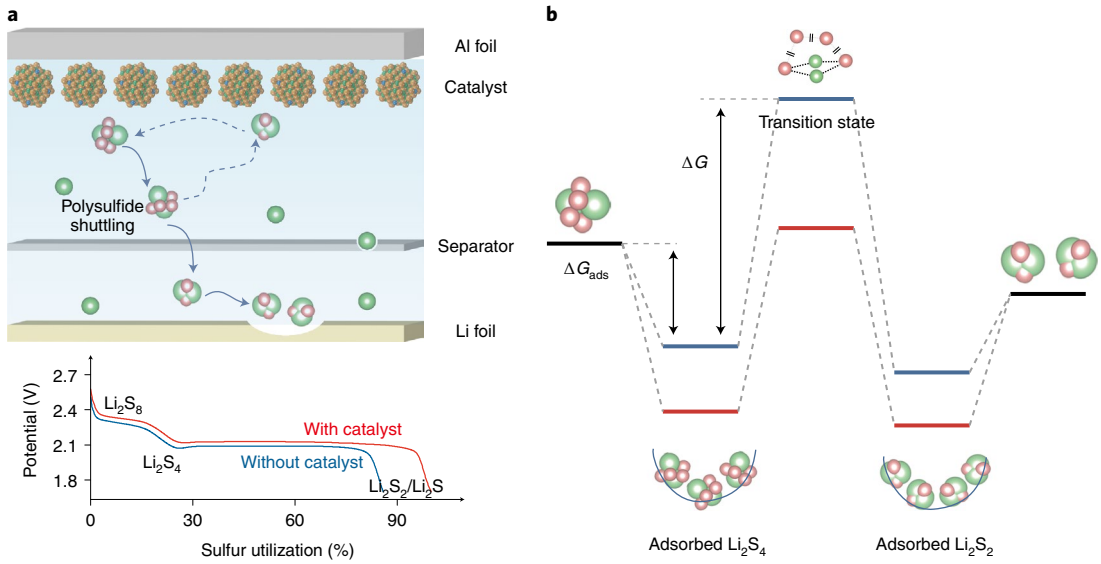

Fig. 1 | Schematic illustration of catalyst design. a, Shuttle effects and catalytic conversion of polysulfides in a Li–S battery. **b**, Simplified activation diagram of liquid–solid conversion between Li_2S_4 and Li_2S_2.

Results

Studies on catalytic activity. To determine the structure–activity relationship, we selected ZnS as the model system because ZnS has a flexible framework to dope. Substitutional cations having different electron affinities are coordinated in stressed tetrahedral sites (Fig. 2a). which modify the *d* bands of the dopants[30]. As sulfur anions of various polysulfides mainly interact with transition-metal cations and their binding energies are coupled to the *d*-band centres (Fig. 2b)[31–34], the activity of cation-doped ZnS is tuned accordingly. Following this strategy, we synthesized $M_{0.125}Zn_{0.875}S$ (M=Mn, Fe, Co, Ni, or Cu) catalysts on reduced graphene oxide (rGO) via a hydrothermal route (see details in Methods). Characterization is shown in Supplementary Note 1, Supplementary Table 1 and Supplementary Figs. 1–10. To analyse the electrocatalytic properties of different $M_{0.125}Zn_{0.875}S$ catalysts, we first loaded the same amount of catalyst on the electrode and conducted electrochemical measurements using symmetric cells within a Li_2S_4-containing electrolyte. Figure 2c shows the cyclic voltammetry (CV) curves of symmetric cells. Upon polarization, Li_2S_4 was converted into higher-order and lower-order polysulfides at the anodes and cathodes, respectively. Among six catalysts, ZnS induces the lowest current response, implying a poor catalytic activity. The dramatic increase in current densities of other cells indicates that dopants in $M_{0.125}Zn_{0.875}S$ accelerate the conversion of polysulfides. A simple comparison of the CV peaks in Fig. 2d shows that from Zn to Mn, the current density first increases and then decreases, showing a volcano-shaped curve. $Co_{0.125}Zn_{0.875}S$ demonstrates the highest current density under the same conditions. The voltage gaps between two coupled anodic and cathodic peaks are usually related to the energy barriers of the conversion reactions (which also affect the reversibility of the reactions)[35]. A small gap indicates a low activation barrier and the enhancement of polysulfide conversion[36]. From Mn to Zn in the 3*d* row of the periodic table, the voltage gap of $M_{0.125}Zn_{0.875}S$ follows an inverted volcano trend, yielding a minimum polarization for $Co_{0.125}Zn_{0.875}S$.

To further confirm the trend, electrochemical impedance spectroscopy (EIS) was conducted to study the kinetics of charge transfer in symmetric cells. The Nyquist plots in Fig. 2e consist of depressed semicircles and linear tails. The diameter of each semicircle is usually proportional to the resistance of charge transfer (R_{CT}) for polysulfide conversion. The $Co_{0.125}Zn_{0.875}S$ cell exhibits the lowest R_{CT}, indicative of the highest catalytic activity. To quantitatively measure the role of catalysts on polysulfide conversion, we assembled $M_{0.125}Zn_{0.875}S$ catalysts into Li–S batteries and obtained the CV curves at various temperatures. Three typical catalysts ($Mn_{0.125}Zn_{0.875}S$, $Co_{0.125}Zn_{0.875}S$ and ZnS) were chosen intentionally from each side and the top of the volcano curve (Fig. 2f–h). Their CV curves show two reduction peaks. A minor peak around 2.3 V is due to the conversion from Li_2S_8 to Li_2S_4, which is a liquid-phase reaction having relatively rapid kinetics. A major peak at 2.0 V corresponds to the liquid–solid conversion from Li_2S_4 to Li_2S_2/Li_2S. Owing to a high energy barrier and slow kinetics, this process is usually the rate-determining step (r.d.s.)[37–40]. Thus, we chose the potentials at 2.065 V (Supplementary Fig. 11) to fit the Arrhenius equation $i \propto A \times e^{-E_a/RT}$, where E_a is the activation energy, R is the gas constant, A is a pre-exponential factor and T is temperature[32,33]. As shown in Fig. 2i, ZnS and $Mn_{0.125}Zn_{0.875}S$ have much higher activation energies of 27.64 and 17.07 kJ mol^{-1}, respectively. By contrast, $Co_{0.125}Zn_{0.875}S$ can reduce the activation barrier of polysulfide conversion down to 13.29 kJ mol^{-1}, indicating the high catalytic activity. Meanwhile, in Supplementary Fig. 12, the voltage gap between anodic and cathodic peaks of $Co_{0.125}Zn_{0.875}S$ is much smaller than those of ZnS and $Mn_{0.125}Zn_{0.875}S$, indicating the improved electrochemical kinetics of $Co_{0.125}Zn_{0.875}S$.

Catalytic mechanism analysis. Polysulfide adsorption was simulated and analysed using density functional theory (DFT, see Supplementary Note 2 for details of model construction). Figure 3a presents the binding energies between three typical polysulfides (Li_2S_2, Li_2S_4 and Li_2S_6) and $M_{0.125}Zn_{0.875}S$ (see details in Methods) using the Perdew–Burke–Ernzerhof (PBE) functional. Geometric configurations are displayed in Supplementary Figs. 13–15. We also calculated the binding energies using the rPBE and PBEsol functionals for comparison (Supplementary Table 2). $Mn_{0.125}Zn_{0.875}S$ has the highest binding energies with the three polysulfides whereas $Cu_{0.125}Zn_{0.875}S$ shows the weakest interaction with polysulfides. The decreasing trend of polysulfide adsorption from $Mn_{0.125}Zn_{0.875}S$ to $Cu_{0.125}Zn_{0.875}S$ seems to contradict their electrocatalytic activities as shown in Fig. 2d. Previous studies usually correlated strong adsorption of polysulfides with a high catalytic activity of polysulfide conversion. However, our calculations indicate that $Mn_{0.125}Zn_{0.875}S$, having the

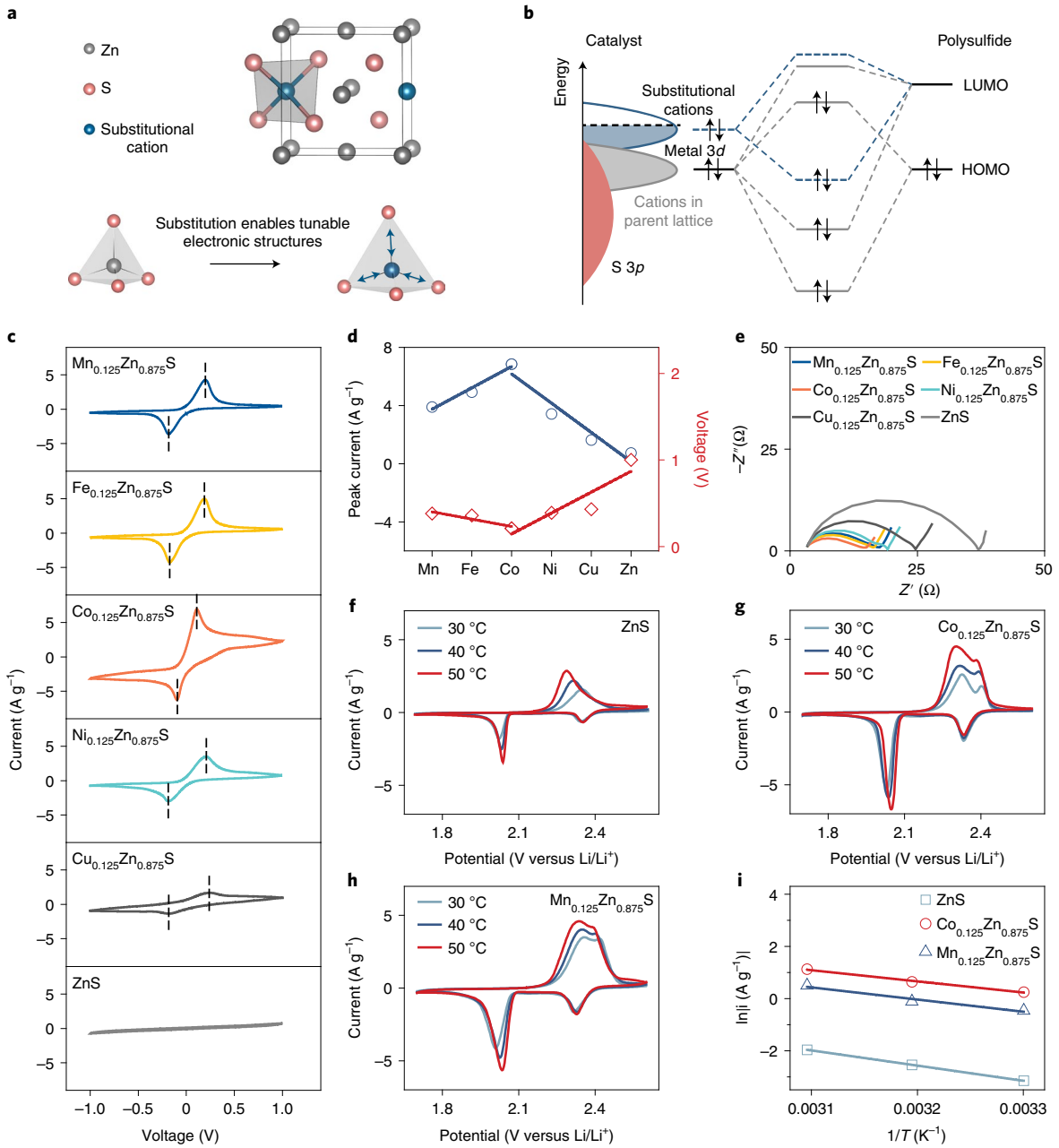

Fig. 2 | Catalyst design and activity characterizations. a, Substitutional ions in a ZnS parent lattice induce tensile or compressive stress, which tunes electronic structures for improving catalysis and adds variety to catalysts beyond simple compounds. **b**, Substitutional cations interact with the lowest unoccupied molecular orbital (LUMO) and highest occupied molecular orbital (HOMO) of polysulfides compared to other cations in parent lattices, showing the tuning principle. **c**, CV curves of symmetric cells using catalysts $M_{0.125}Zn_{0.875}S$ and ZnS at a scan rate of 3 mV s^{-1}. **d**, Voltage gaps between anodic and cathodic CV peaks and peak current of the CV curves of various catalysts. **e**, Nyquist plots of symmetric cells (Z' and Z'' represent the real and imaginary parts of impedance, respectively). **f**–**h**, CV curves of Li–S batteries using ZnS (**d**), $Co_{0.125}Zn_{0.875}S$ (**e**) and $Mn_{0.125}Zn_{0.875}S$ (**f**) as the catalysts in the cathodes (at a scan rate of 0.1 mV s^{-1}). **i**, Arrhenius plots of the three Li–S batteries (*i* is the CV current at 2.065 V).

strongest adsorption to polysulfides, exhibits low catalytic activity. To further confirm the calculations on the adsorption of polysulfides, we added $M_{0.125}Zn_{0.875}S$ powder into a Li_2S_4-containing electrolyte. Figure 3b shows that the Li_2S_4-containing electrolyte was decoloured at an increasing rate from $Cu_{0.125}Zn_{0.875}S$ to $Mn_{0.125}Zn_{0.875}S$. Moreover, ultraviolet–visible (UV–vis) spectroscopic measurements[41,42] further demonstrate that $Mn_{0.125}Zn_{0.875}S$ adsorbed polysulfides more rapidly than $Cu_{0.125}Zn_{0.875}S$. Therefore, our theoretical calculations agree with the visualization and spectroscopic experiments.

The densities of states in Fig. 3c and the partial densities of states in Supplementary Fig. 16 show that the *d*-band centres of transition metals on the (111) surfaces of $M_{0.125}Zn_{0.875}S$ shift upwards to the Fermi level from Cu to Mn, leading to an increasing interaction between polysulfides and $M_{0.125}Zn_{0.875}S$ because more anti-bonding states of M–S bonds can be emptied. Further structural and bonding information was explored and is shown in Fig. 3d–i. Figure 3d presents the molecular configuration of Li_2S_4 on the (111) surface of the $M_{0.125}Zn_{0.875}S$ catalyst. After geometric optimization, two terminal S atoms (S1 and S4) of Li_2S_4 were attached to transition-metal

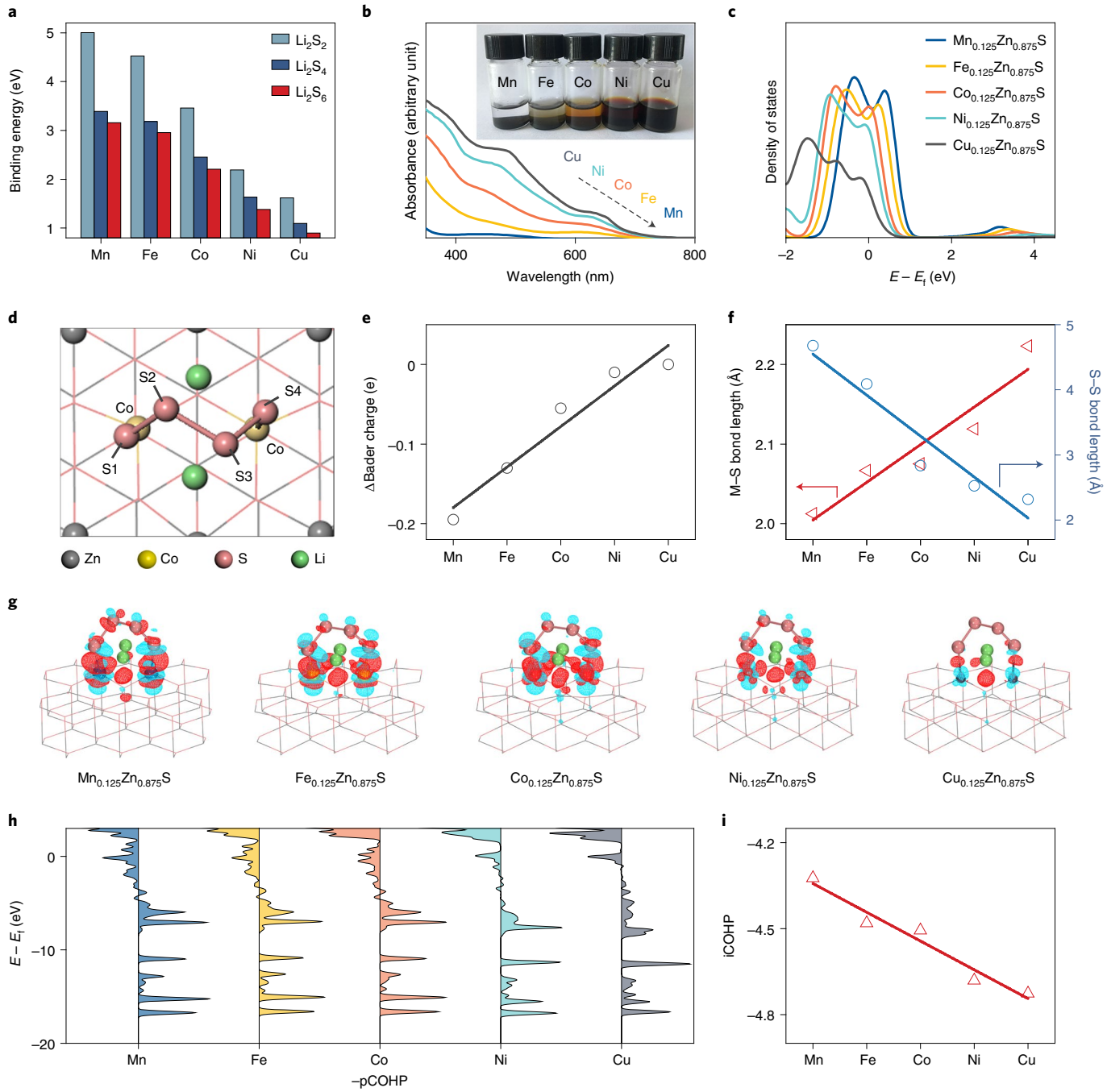

Fig. 3 | Mechanistic studies on catalytic processes. a, Binding energies of Li_2S_2, Li_2S_4 and Li_2S_6 on various catalysts. **b**, UV–vis absorption spectra and visualization tests of the interaction between polysulfides and $M_{0.125}Zn_{0.875}S$ catalysts. a.u., arbitrary unit. **c**, Densities of states of various $M_{0.125}Zn_{0.875}S$ catalysts. **d**, Configuration model of Li_2S_4 on the (111) surface of the $M_{0.125}Zn_{0.875}S$ catalyst. **e**, Bader charge analysis of metal atoms before and after Li_2S_4 adsorption on $M_{0.125}Zn_{0.875}S$ catalysts. **f**, M–S and S–S bond lengths of various $M_{0.125}Zn_{0.875}S$ catalysts. **g**, Electronic density difference (red and blue regions denote the accumulation and depletion of electron density, respectively). **h**,**i**, COHPs (**h**) and iCOHPs (**i**) of Li_2S_4 adsorbed on the (111) surfaces of the $M_{0.125}Zn_{0.875}S$ catalysts.

atoms while two Li ions were attracted to the surface S^{2-} anions of the catalyst, simply owing to electrostatic interactions. As shown in Fig. 3e, Bader charge analysis shows that from Cu to Mn, more electrons are transferred owing to the adsorption of polysulfides, implying stronger adsorption properties. In Fig. 3f and Supplementary Tables 3 and 4, the average length of metal–sulfur (M–S) bonds is shortened from Cu to Mn whereas that of sulfur–sulfur (S1–S2 and S3–S4) bonds is increased. An analysis of electron density difference (Fig. 3g) further reveals that strong adsorption typically induces the electron accumulation between terminal S and surface metal atoms, indicative of a stronger covalence of M–S bonds. Among all substitutional dopants, Mn induces the highest electron density in the middle of M–S bonds. Figure 3h,i presents the projected and integrated crystal orbital Hamilton population (pCOHP and iCOHP) of S1–S2 bonds, respectively[43–45]. From Cu to Mn, more anti-bonding states of S1–S2 bonds shift down below the Fermi level and are filled, indicating that the S1–S2 bonds are weakened. Notably, the iCOHP of S1–S2 bonds increases linearly from Cu to Mn, which is

strongly correlated to the up-shift of *d*-band centres. Supplementary Fig. 17 presents the COHP and iCOHP of M–S, S2–S3 and S3–S4 bonds, showing similar trends.

Interestingly, $Mn_{0.125}Zn_{0.875}S$ induces such a significant electron redistribution that the integrated crystal orbital overlap population (iCOOP) of S1–S2 is close to zero, indicative of a nearly broken bond (Supplementary Fig. 18)[46]. In fact, the distance between S1 and S2 atoms is above 4 Å. Therefore, it may be concluded that the (111) surface of $Mn_{0.125}Zn_{0.875}S$ is so active that it reacts with Li_2S_4 to break S–S bonds directly without the need for electrochemical forces. A high-efficiency catalyst needs an appropriate interaction with polysulfides for lowering the energy barrier of molecular structure transformation instead of directly breaking S–S bonds. As the surface Mn sites would be coordinated by terminal S of Li_2S_4, new Mn–S bonds may passivate the surface and lower the catalytic activity of $Mn_{0.125}Zn_{0.875}S$.

Microkinetic analysis. To further understand how *d*-band centres affect the trend of adsorption and catalysis and explain why $Co_{0.125}Zn_{0.875}S$ has the highest electrocatalytic activity, we analysed the kinetics of the polysulfide conversion reaction on different $M_{0.125}Zn_{0.875}S$ catalysts. Figure 4a presents the calculated binding energies of Li_2S_2 and Li_2S_4 on $M_{0.125}Zn_{0.875}S$ (where each catalyst is represented by using its *d*-band centre of M atoms). As polysulfides generally interact with the *d* band of M atoms, the binding energies of Li_2S_2 and Li_2S_4 depend proportionally on the *d*-band centres of catalyst active sites. Such a linear scaling usually holds for the transition states, further leading to the Brønsted–Evans–Polanyi (BEP) relationship ($E_a = \alpha\Delta E + \beta$)[47–49], which allows for correlating activation energy (E_a) with reaction enthalpy (ΔE) with two undetermined scaling factors (α and β) (Supplementary Fig. 19). The adsorption of Li_2S_4 and desorption of Li_2S_2 can readily be modelled through DFT calculations. However, the conversion from Li_2S_4 to Li_2S_2 involves two electron transfers and a complex configuration change of polysulfide molecules, thereby leading to difficulties in predicting activation energy. To model the kinetics of conversion reactions, we consider three simplified steps and assume reaction (2) or reaction (3) as the r.d.s., respectively.

$$Li_2S_4 + * = Li_2S_4^* \quad (1)$$

$$Li_2S_4^* + 2Li^+ + 2e^- + * = 2Li_2S_2^* \quad (2)$$

$$2Li_2S_2^* = 2Li_2S_2 + 2* \quad (3)$$

The aim of using simplified steps is not to discuss the details of reactions, but to lay out the parameters for fitting the trend of catalytic activity and determining the general principles that govern polysulfide conversion. Reactions (1) and (3) are viewed as the adsorption and desorption steps, respectively. Reaction (2) represents the activation (or dissociation) of polysulfides. The rates of the reactions are expressed as functions of the coverage of Li_2S_4/Li_2S_2 and free sites and they are coupled by several equilibrium constants (see Supplementary Note 3). The rate constants of reactions (2) or (3) are determined by their activation energies that are correlated with the reaction enthalpies through the BEP relationship.

Using the calculated binding energies of polysulfides, we can obtain a volcano plot of reaction rates as shown in Fig. 4b. With the upshift of *d*-band centres from Cu to Mn, the rate increases first and reaches the maximum catalytic activity at $Co_{0.125}Zn_{0.875}S$. When reaction (2) is considered as the r.d.s., the catalytic activity increases from $Cu_{0.125}Zn_{0.875}S$ to $Co_{0.125}Zn_{0.875}S$ owing to the improvement of polysulfide adsorption. The upshift of *d*-band centres from Co to Mn could further enhance the adsorption of polysulfides on catalysts. However, the experimental results in Fig. 2 show decreasing activity, which is in good agreement with the case of reaction (3) as the r.d.s. It is a reasonable conclusion that too strong adhesion of Li_2S_2 to catalysts lowers the coverage of free sites, thereby passivating catalysts. Figure 4c presents the calculated energy diagram of each step (see the fitting details in Supplementary Note 3). The binding energies of Li_2S_4 or Li_2S_2 generally increase from Cu to Mn. However, Li_2S_2 binds more strongly to catalysts than Li_2S_4 does, thereby leading to the formation of the volcano curve. Through modelling it may be concluded that, although the adsorption strength has been widely used to correlate catalytic activity, the binding energy as a descriptor does not always predict activity correctly.

To confirm the passivation, we first conducted CV scans on a rotating disk electrode (RDE) under forced convection. In contrast with symmetric cells and conventional Li–S batteries, forced convection on an RDE enables the continuous replenishment of polysulfide reagents, which minimizes the influence of liquid-phase concentrations. CV curves could mainly represent the catalyst activity upon polarization. As Li reacts with polysulfides, Li metal cannot work as a reference electrode in a polysulfide-containing electrolyte. As shown in the inset of Fig. 4d, we developed a new reference electrode by loading TiO_2 nanoparticles onto the bottom end. Owing to the strong adsorption ability of TiO_2, polysulfide migration was blocked to avoid voltage instability of the reference Li electrode (see details in Methods). Upon polarization, ZnS shows the lowest CV current, indicative of low catalytic activity as compared to $Co_{0.125}Zn_{0.875}S$ (Fig. 4e) and $Mn_{0.125}Zn_{0.875}S$ (Fig. 4f), mainly because of its weak interaction with polysulfides. $Mn_{0.125}Zn_{0.875}S$ delivers an initially high CV current, which dramatically decreases over cycles. After a reversed scan to high voltage (>2.2 V, see Supplementary Note 4 and Supplementary Fig. 20), the high CV current was reproduced in the following cycle (<2.2 V), indicating that the decay over cycles results from passivation instead of catalyst degradation and falling off. Therefore, it is deduced that the strong adsorption of $Mn_{0.125}Zn_{0.875}S$ prevents solid precipitation from being rapidly removed from the surface by forced convection, lowering the availability of the catalytic active sites. For $Co_{0.125}Zn_{0.875}S$, the interaction is medium strength so that the kinetics are accelerated and solid precipitates can be removed promptly. The active sites are not dramatically passivated, leading to high CV current and slow degradation over cycles (a detailed analysis can be found in Supplementary Note 4).

In addition to the RDE analysis, we also measured the ex situ Raman spectra of catalytic layers on the RDEs by rapidly removing the solvents after discharge at 1.7 V. Supplementary Fig. 21 indicates more low-order Li_2S_n and less high-order Li_2S_m on $Co_{0.125}Zn_{0.875}S$ than $Mn_{0.125}Zn_{0.875}S$. However, residual Li_2S was observed on $Mn_{0.125}Zn_{0.875}S$. Analysing the electrolyte residuals in the pores are equal to sampling the reaction products at the last minute. The appearance of Li_2S residual indicates the passivation. We further re-assembled cycled sulfur cathodes with fresh Li and electrolyte. Supplementary Fig. 22 shows that $Mn_{0.125}Zn_{0.875}S$ requires a much higher overpotential (activation barrier) at the beginning of recharge than $Co_{0.125}Zn_{0.875}S$. Despite the high nucleation and charge capacity, $Co_{0.125}Zn_{0.875}S$ does not exhibit an envelope-like overpotential (a voltage jump) at the beginning of recharge, indicative of high catalytic activity (see discussion below Supplementary Fig. 22). These observations lead us to conclude that the passivation slows down the catalysis on $Mn_{0.125}Zn_{0.875}S$.

Figure 4g–i presents an illustrated summary. A weak adsorption (Fig. 4g) allows polysulfides to diffuse towards anodes whereas strong adsorption (Fig. 4h) readily facilitates the breaking of S–S bonds and may passivate the catalysts. Only appropriate adsorption (Fig. 4i) could accelerate the polysulfide conversion. As polysulfide adsorption on catalysts was proportionally correlated to the same *d*-band centres, the enhancement effect for Li_2S_4 conversion may in turn hinder the desorption of Li_2S_2.

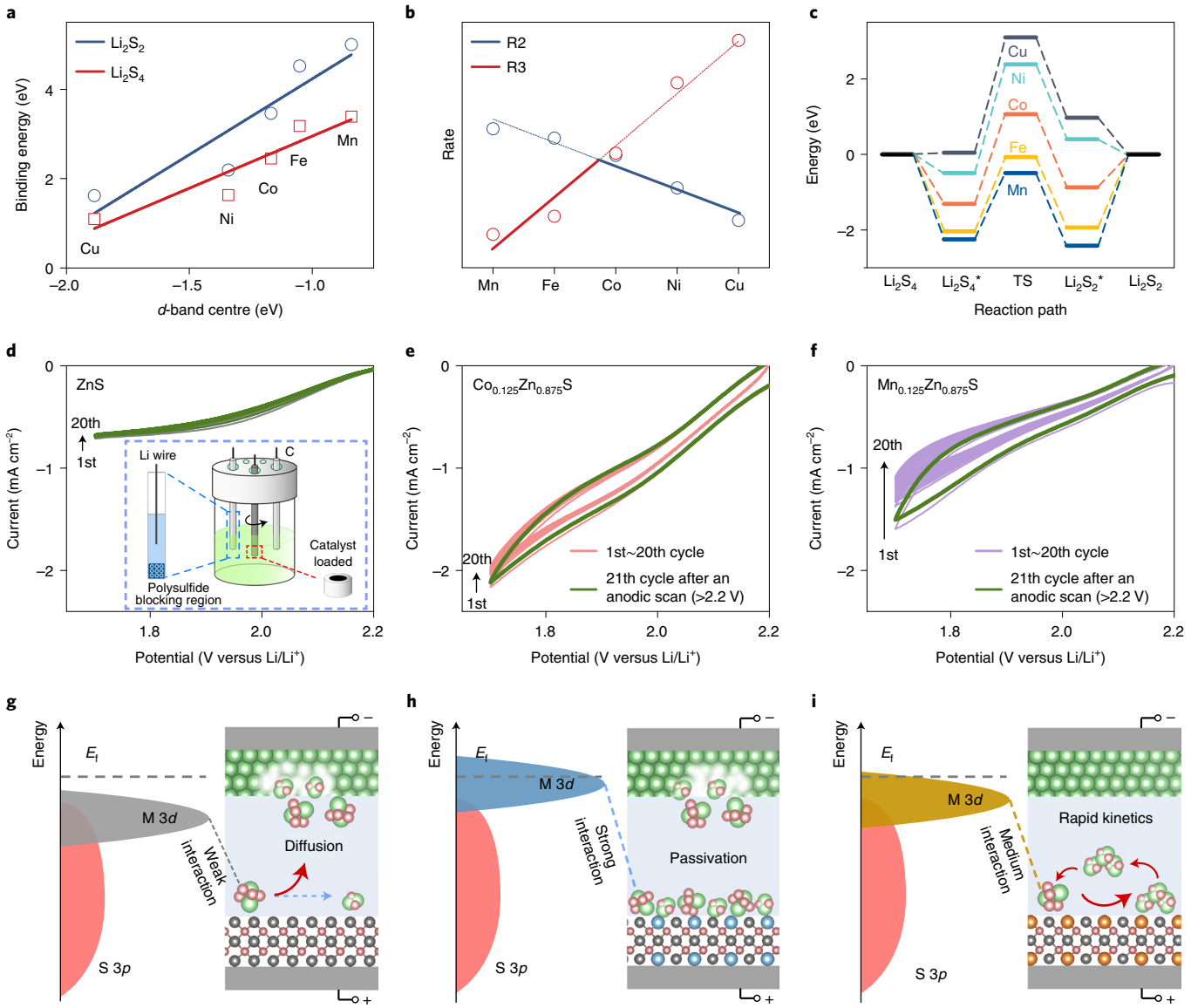

Fig. 4 | Kinetic analysis of polysulfide conversion on catalyst surface. a, Relationship of binding energy to *d*-band centre. **b**, Volcano plots of rates with respect to different dopants (the blue and red lines represent reactions (2) or (3) (R2 and R3) as the r.d.s., respectively). **c**, Reaction energy diagram from Li_2S_4 to Li_2S_2. **d–f**, CV curves of ZnS (**d**), $Co_{0.125}Zn_{0.875}S$ (**e**) and $Mn_{0.125}Zn_{0.875}S$ (**f**) at 50 mV s^{-1} and 1,000 r.p.m. The inset in **d** is an illustration of the RDE setup using a Li reference electrode. **g–i**, Schematic illustrationa of weak (**g**), strong (**h**) and medium (**i**) interactions of polysulfides with catalysts.

Experimental and theoretical analyses demonstrate that, through the *d*-band tuning strategy, $Co_{0.125}Zn_{0.875}S$ was found to be an excellent catalyst for polysulfide conversion. It should be noted that in $Co_{0.125}Zn_{0.875}S$, Co^{2+} is coordinated with four S^{2-} in tetrahedral sites, which may be also realized in the Co–S binary system. Especially, Co_3S_4 has tetrahedral CoS_4 units. Furthermore, we compared the catalytic activities of $Co_{0.125}Zn_{0.875}S$ with CoS_2 and Co_3S_4. Despite the low Co doping, $Co_{0.125}Zn_{0.875}S$ shows much higher CV response (Supplementary Fig. 23) and lower impedance of charge transfer (Supplementary Fig. 24) than CoS_2 and Co_3S_4, indicating that using the lattice stress of dopants in the ZnS parent matrix could realize higher catalytic activity that a pure Co–S binary system could not achieve. Therefore, the revealed principles further broaden the options of polysulfide catalysts and offer rational design of catalysts.

Electrochemical properties of Li–S batteries. Figure 5 shows the electrochemical properties of Li–S batteries using the designed catalysts. Due to the improved catalytic activity, $Co_{0.125}Zn_{0.875}S$ (Fig. 5a) delivered the highest capacity of 1,426.3 mAh g^{-1} among all the $M_{0.125}Zn_{0.875}S$ catalysts at 0.1C. Figure 5b summarizes polarization overpotentials at half capacity and nucleation overpotentials at the beginning of 2.1 V plateaus. Either of these two overpotentials is usually considered as a measure of kinetics. $Co_{0.125}Zn_{0.875}S$ is at the bottom of the inverted volcano, showing the lowest polarization and nucleation overpotentials. Figure 5c presents the EIS measurements of Li–S batteries using $M_{0.125}Zn_{0.875}S$ catalysts. The smallest diameter for $Co_{0.125}Zn_{0.875}S$ confirms its highest catalytic activity. To explain the depressed semicircles, the Nyquist plots were fitted using the equivalent circuit including two resistor-capacitor (RC) circuits (where capacitors are replaced by constant phase element (CPE), see Supplementary Fig. 25). The first RC component (R_{surf}/CPE1) in the high-frequency range is related to the resistance (R_{surf}) and capacitance (CPE1) of the solid electrolyte interphase (SEI) layer on the sulfur cathode and Li metal. The R_{ct}/CPE2 component in the low-frequency range is usually attributed to the charge transfer (R_{ct}) at the interfaces of the S cathodes. By comparing their rates

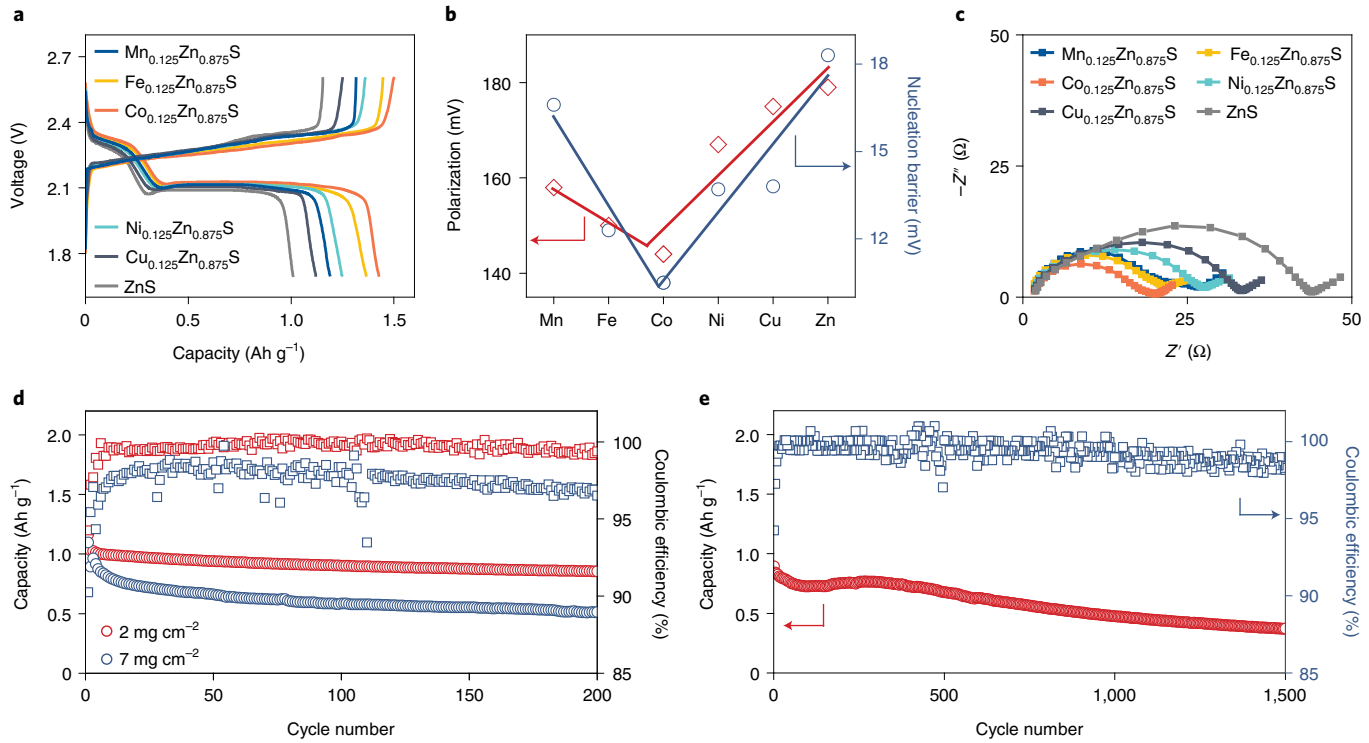

Fig. 5 | Electrochemical properties of Li–S batteries using $M_{0.125}Zn_{0.875}S$ catalysts. a, Galvanostatic charge–discharge curves (at 0.1C) for Li–S batteries with a sulfur loading of 2 mg cm^{-2}. **b**, Polarization overpotentials between charge and discharge curves at half capacity and nucleation overpotentials at the beginning of 2.1 V plateaus. **c**, Nyquist curves for Li–S batteries using $M_{0.125}Zn_{0.875}S$ catalysts at 1.7 V. **d**, Cycling properties of two $Co_{0.125}Zn_{0.875}S$-catalysed Li–S batteries with low and high S loadings, respectively. **e**, Long-term cycling properties of a $Co_{0.125}Zn_{0.875}S$-catalysed Li–S battery with an S loading of 2 mg cm^{-2} at 2C.

and cycling properties in Supplementary Fig. 26 and Supplementary Fig. 27, $Co_{0.125}Zn_{0.875}S$ shows better capacity retention than other $M_{0.125}Zn_{0.875}S$ catalysts. Based on the above analysis, $Co_{0.125}Zn_{0.875}S$ demonstrates the advantages for catalysing Li–S batteries. Figure 5d presents the cycling performance at low and high S loadings (2 and 7 mg cm^{-2}). These two Li–S batteries show similar initial Coulombic efficiencies (CEs) of 94.3 and 90.4%, which gradually increase to 99.5 and 98.1% after 10 and 20 cycles, respectively. The low S loading cell can deliver a high initial specific capacity of 1,163.2 mAh g^{-1} and retain a capacity as high as 856.1 mAh g^{-1} at 1C after 200 cycles whereas the high S loading cell shows a capacity of 1,098.5 mAh g^{-1} at the beginning and this decreases to 513.2 mAh g^{-1} in the 200th cycle. Figure 5e shows that at 2C, the $Co_{0.125}Zn_{0.875}S$-catalysed Li–S batteries could deliver a capacity of 482.5 mAh g^{-1} even after 1,500 cycles with a capacity decay as low as 0.033% per cycle.

To examine the shuttle effect, we conducted a post-mortem analysis of Li metal anodes, which were disassembled from Li–S batteries (after 100 cycles). Supplementary Fig. 28a–c shows that $Co_{0.125}Zn_{0.875}S$ leads to a much smoother surface of Li metal anode than ZnS or $Mn_{0.125}Zn_{0.875}S$. The rough surface was partly due to the migrated polysulfides that react immediately with active Li metal. The energy dispersive X-ray (EDX) mapping images in Supplementary Fig. 28d–f confirm that more S signals were received from the surface of Li metal anodes of ZnS and $Mn_{0.125}Zn_{0.875}S$ cells. This implies that polysulfides were not converted effectively in the cathodes during cycling. The resulting migration of polysulfides towards the anodes lowers the deliverable capacity.

Discussion

During charge/discharge, S species in Li–S batteries change their polarities and molecular geometries, giving rise to a wide range of adsorption energies. It would be rather complicated to determine the relationship between each polysulfide adsorption and overall conversion rate for a specific catalyst. Fortunately, the DFT calculations reveal that the binding energies of most polysulfides are proportional to the *d*-band centres of the active surface sites. In conjunction with the BEP relationship, we can fit the microkinetics of polysulfide conversion and reveal a volcano-like trend of catalytic activities with respect to the binding energies of polysulfides.

In addition, 16 electrons are transferred in Li–S batteries through sequential reactions from solid S, to soluble polysulfides and finally to solid Li_2S_2/Li_2S. Two solid species at the end of charge/discharge increase the risk of passivating the catalytic sites. Previously, strengthening the adsorption of polysulfides was usually focused upon tackling the shuttle effects whereas the removal of solid products from active sites was seldom considered. This work demonstrates that passivation caused by strong adsorption of Li_2S_2/Li_2S may become the limiting factor for catalytic activity. Nevertheless, the anchoring of polysulfides benefits from strong adsorption, partly suppressing the polysulfide shuttling. Therefore, tuning the adsorption of polysulfides leads to multiple effects, which should be considered together for building better Li–S batteries.

In summary, we report a fundamental principle about tuning the adsorption of polysulfides to design highly efficient catalysts for Li–S batteries. By substituting cations of a parent ZnS lattice, the varying electron affinities of 3*d* dopants (Mn^{2+}, Fe^{2+}, Co^{2+}, Ni^{2+} or Cu^{2+}) and lattice stress could shift the *d*-band centres of active sites and adjust their interaction with the frontier orbitals of polysulfides. More importantly, a volcano relationship between polysulfide adsorption and catalytic activity was revealed experimentally and confirmed theoretically for Li–S systems. Strengthening adsorption to enhance catalytic activity may in turn decelerate the polysulfide conversion when desorption of discharged polysulfides (Li_2S_2/Li_2S) is rate limiting. Polysulfide passivation was found to play a critical

role in catalysis. Some catalysts that were considered inert may instead be too active and deserve re-examination. Using the tuning principles, we developed a highly efficient catalyst, $Co_{0.125}Zn_{0.875}S$, and demonstrated superior catalytic activity that is not achieved by simple binary compounds. The concepts revealed in this work offer a rational basis for understanding the catalytic process at the atomic and molecular levels and designing new catalysts for Li–S batteries.

Methods

Preparation of catalysts. Approximately 17.5 mg graphene oxide (GO) was first dispersed in 35 ml ethylene glycol. After sonication for 12 h, 0.55 g polyacrylic acid (M_w = 2,000), 1.50 mmol thiourea and a variety of acetates were dissolved in the suspension. To vary the cations in ZnS, about 0.7 mmol Zn^{2+} and 0.1 mmol M^{2+} (Mn^{2+}, Fe^{2+}, Co^{2+}, Ni^{2+} or Cu^{2+}) were added in the form of acetates. After vigorously stirring for 30 min, the suspension was transferred to a Teflon-lined stainless steel autoclave and heated at 180 °C for 20 h. The as-obtained precipitates were washed with de-ionized water and ethanol and then re-dispersed in 35 ml de-ionized water. A freeze-drying procedure was followed to remove water and form a powder precursor. After heat treatment at 600 °C for 2 h in Ar gas, the precursor catalysts were converted into catalysts (labelled as $rGO/M_{0.125}Zn_{0.875}S$).

Characterization of materials. X-ray diffraction patterns were obtained on a Rigaku Ultimate IV using Cu Kα radiation. The Brunauer–Emmett–Teller surface areas were measured on a Kubo X1000 analyser. The morphologies of the materials were examined using a field emission scanning electron microscope (SEM, Zeiss, Gemini500) and a transmission electron microscope (TEM, FEI, Tecnai F20 and JEOL, JEM-F200).

Preparation of Li reference electrode. A wire of Li metal was inserted into a glass tube filled with a baseline electrolyte that consisted of 1 M bis(trifluoromethane) sulfonimide lithium (LiTFSI) in a 1:1 volume ratio solution of 1,2-dimethoxyethane (DME) and 1,3-dioxolane (DOL) with 1% $LiNO_3$. The bottom end of the glass tube was loaded with porous ceramic to separate the internal electrolyte from the external electrolyte. The pores of the ceramic were filled with a mixture (9:1 mass ratio) of TiO_2 and polyvinylidene fluoride (PVDF) to inhibit polysulfide diffusion from the external electrolyte (see the inset of Fig. 4d).

Symmetric cell tests. Li_2S_4 (20 mg ml^{-1}) was added to the baseline electrolyte for the symmetric cell tests. Electrodes of the symmetric cells were prepared by coating Al foils with a mixture of 50 wt% $rGO/M_{0.125}Zn_{0.875}S$, 40 wt% Super-P and 10 wt% PVDF in *N*-methylpyrrolidone (NMP). The loading mass of catalysts was 2 mg cm^{-2}. The catholyte/catalyst ratio in the symmetric cells was 10 µl mg^{-1}. Coin cells (CR2032, MTI) were assembled in an Ar-filled glove box.

Preparation of polysulfide adsorption test. Li_2S_4 (2 mg ml^{-1}) was first synthesized by mixing the stoichiometric ratio of Li_2S to sulfur in DME. Then, catalyst powder was added to the Li_2S_4/DME solution for visual comparison.

Passivation tests. An RDE was used to conduct passivation tests (Φ3mm, BAS Inc). Catalysts (4 mg) were dispersed in a mixture of 500 µl de-ionized water and 500 µl ethanol. After adding 17 µl Nafion, the suspension was ultrasonicated for 30 min. Then, 5 µl of catalyst solution was dropped onto a polished RDE. The counter electrode was carbon. Li_2S_4 (0.01 M) was added to the baseline electrolyte for passivation tests. All measurements were conducted inside an Ar-filled glovebox.

Electrochemical characterizations of Li–S batteries. S was impregnated into $rGO/M_{0.125}Zn_{0.875}S$ using a melt-diffusion method at 155 °C for 10 h according to previous reports. The resultant $S\text{-}rGO/M_{0.125}Zn_{0.875}S$ (80 wt%) powder was mixed with 10 wt% Super-P and 10 wt% PVDF in NMP to form a slurry, which was then cast onto Al foil and vacuum dried at 60 °C. The S loadings were controlled at around 2 and 7 mg cm^{-2}. The sulfur ratio in the catalyst/sulfur composite was 70% for low S loading and 90% for high S loading. S cathodes were assembled with Li foil into coin cells in an Ar-filled glove box. About 10 µl mg^{-1} baseline electrolyte was used for the low S loading (2 mg cm^{-2}) and 5 µl mg^{-1} was used for the high S loading (7 mg cm^{-2}). Nyquist plots were obtained at 1.7 V after the 20th charge–discharge cycle to allow batteries to reach a relatively stable state at 0.1C. Specific capacities were based on the mass of elemental S. CV, galvanostatic charge–discharge and EIS measurements (100 kHz to 0.1 Hz) were carried out on a battery tester (Lanhe, CT2001A) and a potentiostat (VSP, Bio-Logic).

DFT calculations. Spin-polarized DFT calculations were performed using CASTEP (Cambridge Serial Total Package). The electron exchange and correlation interactions were described using the Perdew–Burke–Ernzerhof functional in the generalized gradient approximation[50]. For comparison, other functionals such as rPBE and PBEsol were used to calculate binding energies and geometric configurations of Li_2S_4 molecules adsorbed on $M_{0.125}Zn_{0.875}S$ surfaces. A cutoff energy of 500 eV was employed for all calculations. For the surface adsorption model, the Brillouin zone was sampled using a 3×2×1 *k*-point mesh. The total energy convergence and the forces on each atom were set to be lower than 10^{-5} eV and 0.05 eV A^{-1}, respectively. The DFT + *U* method was used for all calculations and the *U* values for Mn, Fe, Co and Ni were set to 3.6, 4.6, 5.0 and 5.1 eV, respectively. The binding energy (E_b) of a polysulfide on a cleaved surface of the catalyst was calculated as follows:

$$E_b = E_{surf} + E_{ps} - E_{ps@surf} \quad (4)$$

where E_{surf} is the energy of the cleaved surface, E_{ps} is the energy of the isolated polysulfide and $E_{ps@surf}$ is the energy of the polysulfide adsorbed on the cleaved surface. The binding energies were calculated on the most exposed (111) surface of the catalyst.

The *d*-band centre (ε_d) of a transition metal was calculated as follows:

$$\varepsilon_d = \frac{\int_{-\infty}^{E_f} E \times f(E)\,dE}{\int_{-\infty}^{E_f} f(E)\,dE} \quad (5)$$

where $f(E)$ is the density of states and E_f is the energy of the Fermi level.

Data availability

Source data are provided with this paper. All other data are available from the authors upon reasonable request.

Received: 12 December 2020; Accepted: 7 May 2022;
Published online: 16 June 2022

References

1. Pu, J. et al. Electrodeposition technologies for Li-based batteries: new frontiers of energy storage. *Adv. Mater.* **32**, 1903808 (2019).
2. Ji, X., Lee, K. T. & Nazar, L. F. A highly ordered nanostructured carbon–sulphur cathode for lithium–sulphur batteries. *Nat. Mater.* **8**, 500–506 (2009).
3. Chu, H. et al. Achieving three-dimensional lithium sulfide growth in lithium-sulfur batteries using high-donor-number anions. *Nat. Commun.* **10**, 188 (2019).
4. Pang, Q. et al. Tuning the electrolyte network structure to invoke quasi-solid state sulfur conversion and suppress lithium dendrite formation in Li–S batteries. *Nat. Energy* **3**, 783–791 (2018).
5. Pu, J. et al. Conductivity and lithiophilicity gradients guide lithium deposition to mitigate short circuits. *Nat. Commun.* **10**, 1896 (2019).
6. Jin, X. et al. Interfacial design principle of sodiophilicity-regulated interlayer deposition in a sandwiched sodium metal anode. *Energy Storage Mater.* **31**, 221–229 (2020).
7. Sun, Z. et al. Conductive porous vanadium nitride/graphene composite as chemical anchor of polysulfides for lithium-sulfur batteries. *Nat. Commun.* **8**, 14627 (2017).
8. Gao, X. et al. Incorporating the nanoscale encapsulation concept from liquid electrolytes into solid-state lithium–sulfur batteries. *Nano Lett.* **20**, 5496–5503 (2020).
9. Zhang, L. et al. Enhanced polysulfide regulation via porous catalytic V_2O_3/V_8C_7 heterostructures derived from metal-organic frameworks toward high-performance Li–S batteries. *ACS Nano* **14**, 8495–8507 (2020).
10. Baumann, A. E., Han, X., Butala, M. M. & Thoi, V. S. Lithium thiophosphate functionalized zirconium MOFs for Li–S batteries with enhanced rate capabilities. *J. Am. Chem. Soc.* **141**, 17891–17899 (2019).
11. Wang, L. et al. To effectively drive the conversion of sulfur with electroactive niobium tungsten oxide microspheres for lithium–sulfur battery. *Nano Energy* **77**, 105173 (2020).
12. Wang, Z.-Y., Wang, L., Liu, S., Li, G.-R. & Gao, X.-P. Conductive CoOOH as carbon-free sulfur immobilizer to fabricate sulfur-based composite for lithium–sulfur battery. *Adv. Funct. Mater.* **29**, 1901051 (2019).
13. Wu, W. et al. Biomimetic bipolar microcapsules derived from *Staphylococcus aureus* for enhanced properties of lithium–sulfur battery cathodes. *Adv. Energy Mater.* **8**, 1702373 (2018).
14. Yang, X. et al. Promoting the transformation of Li_2S_2 to Li_2S: significantly increasing utilization of active materials for high-sulfur-loading Li–S batteries. *Adv. Mater.* **31**, 1901220 (2019).
15. Wang, Z. et al. Self-supported and flexible sulfur cathode enabled via synergistic confinement for high-energy-density lithium–sulfur batteries. *Adv. Mater.* **31**, 1902228 (2019).
16. Yao, Y. et al. A dual-functional conductive framework embedded with TiN-VN heterostructures for highly efficient polysulfide and lithium regulation toward stable Li–S full batteries. *Adv. Mater.* **32**, 1905658 (2019).
17. Wang, R. et al. Highly dispersed cobalt clusters in nitrogen-doped porous carbon enable multiple effects for high-performance Li–S battery. *Adv. Energy Mater.* **10**, 1903550 (2020).

18. Zhou, G. M. et al. Catalytic oxidation of Li_2S on the surface of metal sulfides for Li–S batteries. *Proc. Natl Acad. Sci. USA* **114**, 840–845 (2017).
19. Zhang, Z., Kong, L.-L., Liu, S., Li, G.-R. & Gao, X.-P. A high-efficiency sulfur/carbon composite based on 3D graphene nanosheet@carbon nanotube matrix as cathode for lithium–sulfur battery. *Adv. Energy Mater.* **7**, 1602543 (2017).
20. Lin, H. et al. Electrocatalysis of polysulfide conversion by sulfur-deficient MoS_2 nanoflakes for lithium–sulfur batteries. *Energy Environ. Sci.* **10**, 1476–1486 (2017).
21. Al Salem, H., Babu, G., Rao, C. V. & Arava, L. M. R. Electrocatalytic polysulfide traps for controlling redox shuttle process of Li–S batteries. *J. Am. Chem. Soc.* **137**, 11542–11545 (2015).
22. Wang, H. et al. A lithium-sulfur battery with a solution-mediated pathway operating under lean electrolyte conditions. *Nano Energy* **76**, 105041 (2020).
23. Peng, L. et al. A fundamental look at electrocatalytic sulfur reduction reaction. *Nat. Catal.* **3**, 762–770 (2020).
24. Xue, W. et al. Intercalation-conversion hybrid cathodes enabling Li–S full-cell architectures with jointly superior gravimetric and volumetric energy densities. *Nat. Energy* **4**, 374–382 (2019).
25. Wang, Y. et al. Enhancing catalytic activity of titanium oxide in lithium–sulfur batteries by band engineering. *Adv. Energy Mater.* **9**, 1900953 (2019).
26. Zhou, J. et al. Deciphering the modulation essence of p bands in Co-based compounds on Li-S chemistry. *Joule* **2**, 2681–2693 (2018).
27. Seo, S. D., Park, D., Park, S. & Kim, D. W. "Brain-coral-like" mesoporous hollow CoS_2@N-doped graphitic carbon nanoshells as efficient sulfur reservoirs for lithium–sulfur batteries. *Adv. Funct. Mater.* **29**, 1903712 (2019).
28. Pu, J. et al. Multifunctional Co_3S_4@sulfur nanotubes for enhanced lithium-sulfur battery performance. *Nano Energy* **37**, 7–14 (2017).
29. Liu, Y. et al. Nitrogen doping improves the immobilization and catalytic effects of Co_9S_8 in Li-S batteries. *Adv. Funct. Mater.* **30**, 2002462 (2020).
30. Kitchin, J. R., Norskov, J. K., Barteau, M. A. & Chen, J. G. Role of strain and ligand effects in the modification of the electronic and chemical properties of bimetallic surfaces. *Phys. Rev. Lett.* **93**, 156801 (2004).
31. Zhang, Y. et al. Hierarchical defective $Fe_{3-x}C$@C hollow microsphere enables fast and long-lasting lithium–sulfur batteries. *Adv. Funct. Mater.* **30**, 2001165 (2020).
32. Shen, Z. et al. Efficient $Ni_2Co_4P_3$ nanowires catalysts enhance ultrahigh-loading lithium–sulfur conversion in a microreactor-like battery. *Adv. Funct. Mater.* **30**, 1906661 (2020).
33. Shen, Z. et al. Rational design of a $Ni_3N_{0.85}$ electrocatalyst to accelerate polysulfide conversion in lithium–sulfur batteries. *ACS Nano* **14**, 6673–6682 (2020).
34. Shen, J. et al. Mechanistic understanding of metal phosphide host for sulfur cathode in high-energy-density lithium–sulfur batteries. *ACS Nano* **13**, 8986–8996 (2019).
35. Wang, R. et al. Bidirectional catalysts for liquid–solid redox conversion in lithium–sulfur batteries. *Adv. Mater.* **32**, 2000315 (2020).
36. Li, R. et al. Sandwich-like catalyst–carbon–catalyst trilayer structure as a compact 2D host for highly stable lithium–sulfur batteries. *Angew. Chem. Int. Ed.* **59**, 12129–12138 (2020).
37. Zhou, D. et al. Polyolefin-based Janus separator for rechargeable sodium batteries. *Angew. Chem. Int. Ed.* **59**, 2–12 (2020).
38. Ye, H., Li, M., Liu, T., Li, Y. & Lu, J. Activating Li_2S as the lithium-containing cathode in lithium–sulfur batteries. *ACS Energy Lett.* **5**, 2234–2245 (2020).
39. Zeng, P. et al. Enhanced catalytic conversion of polysulfides using bimetallic Co_7Fe_3 for high-performance lithium–sulfur batteries. *ACS Nano* **14**, 11558–11569 (2020).
40. Wang, W., Wang, D., Wang, G., Zheng, M. & Wang, G. Elastic, conductive coating layer for self-standing sulfur cathode achieving long lifespan Li–S batteries. *Adv. Energy Mater.* **10**, 1904026 (2020).
41. Zhang, D. et al. Catalytic conversion of polysulfides on single atom zinc implanted MXene toward high-rate lithium–sulfur batteries. *Adv. Funct. Mater.* **30**, 2002471 (2020).
42. Luo, L., Li, J., Asl, H. Y. & Manthiram, A. In-situ assembled VS_4 as a polysulfide mediator for high-loading lithium–sulfur batteries. *ACS Energy Lett.* **5**, 1177–1185 (2020).
43. Dronskowski, R. & Bloechl, P. E. Crystal orbital Hamilton populations (COHP): energy-resolved visualization of chemical bonding in solids based on density-functional calculations. *J. Phys. Chem.* **97**, 8617–8624 (1993).
44. Deringer, V. L., Tchougréeff, A. L. & Dronskowski, R. Crystal orbital Hamilton population (COHP) analysis as projected from plane-wave basis sets. *J. Phys. Chem. A* **115**, 5461–5466 (2011).
45. Wei, T.-R. et al. Exceptional plasticity in the bulk single-crystalline van der Waals semiconductor InSe. *Science* **369**, 542–545 (2020).
46. Schubert, B., Avouris, P. & Hoffmann, R. A theoretical study of the initial stages of Si(111)-7×7 oxidation. II. The dissociated state and formation of SiO_4. *J. Chem. Phys.* **98**, 7606–7612 (1993).
47. van Santen, R. A., Neurock, M. & Shetty, S. G. Reactivity theory of transition-metal surfaces: a Brønsted–Evans–Polanyi linear activation energy–free-energy analysis. *Chem. Rev.* **110**, 2005–2048 (2010).
48. Cheng, J. et al. Brønsted–Evans–Polanyi relation of multistep reactions and volcano curve in heterogeneous catalysis. *J. Phys. Chem. C.* **112**, 1308–1311 (2008).
49. Bligaard, T. et al. The Brønsted–Evans–Polanyi relation and the volcano curve in heterogeneous catalysis. *J. Catal.* **224**, 206–217 (2004).
50. Perdew, J. P., Burke, K. & Ernzerhof, M. Generalized gradient approximation made simple. *Phys. Rev. Lett.* **77**, 3865–3868 (1996).

Acknowledgements

We acknowledge the financial support of the National Key Research and Development Program of China (2020YFA0406104) and the National Natural Science Foundation of China (22075131). The numerical calculations were carried out at the computing facilities in the High-Performance Computing Center (HPCC) of Nanjing University. Work at Argonne National Laboratory was supported by the US Department of Energy (DOE), Office of Energy Efficiency and Renewable Energy, Vehicle Technologies Office under the US-China Clean Energy Research Center (CERC-CVC2) programme. Argonne National Laboratory is operated for the DOE Office of Science by UChicago Argonne, LLC, under contract number DE-AC02-06CH11357.

Author contributions

H.Z. and Z.S. conceived the idea and designed the project. Z.S., X.J. and J.T. performed the catalyst synthesis and carried out the electrochemical experiments. Z.S., M.L., Y.Y. and S.Z. conducted the morphology and structural characterizations. Z.S., H.Z. and X.J. conducted the DFT calculations and microkinetic modelling. S.F., X.F., W.X. and H.L. assisted with the the ex situ Raman measurements and analysed the spectra. H.Z. and J.L. supervised the project and wrote the manuscript. All authors analysed the data and discussed the results.

Competing interests

The authors declare no competing interests.

Additional information

Supplementary information The online version contains supplementary material available at https://doi.org/10.1038/s41929-022-00804-4.

Correspondence and requests for materials should be addressed to Jun Lu or Huigang Zhang.

Peer review information *Nature Catalysis* thanks Mahbub Islam, Harry Hoster and Qianfan Zhang for their contribution to the peer review of this work.